Progress in Additive Manufacturing
https://doi.org/10.1007/s40964-025-01057-w

FULL RESEARCH ARTICLE

Mono-material sandwich structures design produced by Foam Additive Manufacturing: study of performances under dynamic conditions

Daniele Rizzo[2] · Gabriella Epasto[2] · Andrea Lorenzo Henri Sergio Detry[1,3] · Luca Landolfi[4] · Ilaria Papa[1] · Antonino Squillace[1]

Received: 3 October 2024 / Accepted: 6 March 2025
© The Author(s) 2025

Abstract

The growing demand for environmentally friendly and lightweight solutions in structural applications highlights the importance of research for innovative materials and design methods to satisfy rigorous performance requirements. This research investigates the potential of the Foam Additive Manufacturing (FAM) process to create sustainable, high-impact-resistant materials. Foamed PLA specimens with tailored core densities were evaluated under low-velocity impact conditions, demonstrating up to 127% higher perforation energy than honeycomb infill structures of similar density. Sustainability in this approach stems from the use of biodegradable PLA, the avoidance of chemical blowing agents through the adoption of CO_2 as a physical blowing agent, and the mono-material design, which facilitates recycling at the end of the product lifecycle. Additionally, the lightweight nature of the foamed structures reduces material consumption and enhances energy efficiency during use, particularly in applications requiring weight minimization. Detailed failure mode analyses revealed that foamed specimens absorb energy more efficiently due to mechanisms such as core indentation and foam cell collapse, achieving specific energy absorption (SEA_{ρ}) values up to 0.06 [$Jm^3\ kg^{-1}$] for low-density specimen. Furthermore, based on the correlation between impact energy and sandwich density, the failure mode map highlights the superior impact resistance and progressive failure mechanisms of foamed specimens. These findings demonstrate the potential of FAM to bridge the gap between sustainability and performance, paving the way for innovative applications in fields such as packaging, automotive, and aerospace.

✉ Andrea Lorenzo Henri Sergio Detry
andrea.detry@unina.it

1 Department of Chemical, Materials, and Industrial Production Engineering, University of Naples Federico II, Piazzale Vincenzo Tecchio, 80, Naples, Italy

2 Department of Engineering, University of Messina, Contrada Di Dio - Vill. Sant'Agata, Messina, Italy

3 Center for Complexity and Biosystems, Department of Physics, University of Milan, 20133, Milan, Italy

4 Department of Management, Information and Production Engineering, University of Bergamo, Via Pasubio 7B Dalmine, Bergamo, Italy

Published online: 29 April 2025

Graphic abstract

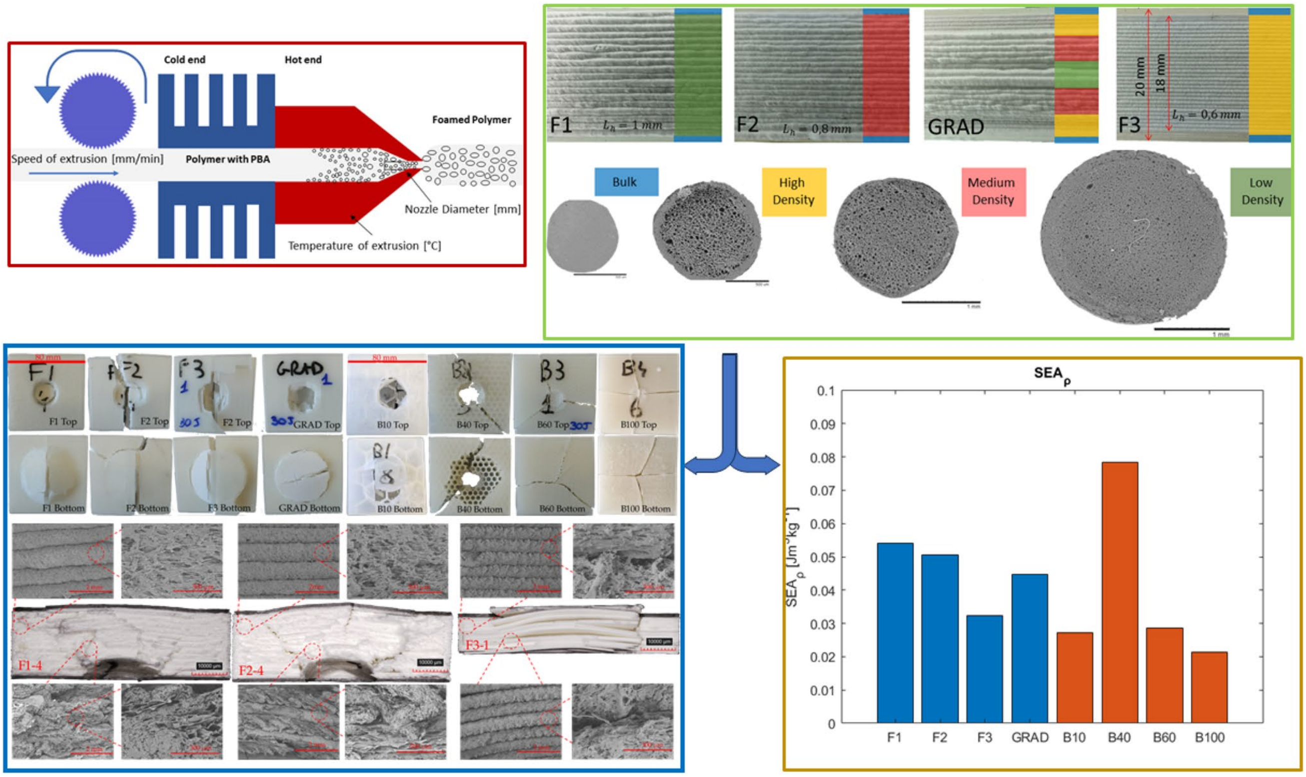

Keywords Foam Additive Manufacturing · Manufacturing science · Polymeric foam · Material design · Low-velocity impact

Abbreviations

3D	Three dimensional
B	Un-foamed specimens
AM	Additive manufacturing
BFP	Bottom face perforation
CFR	Carbon fiber reinforced
CFRP	Carbon fiber reinforced polymers
CO_2	Carbon dioxide
F	Foamed specimens
FAM	Foam Additive Manufacturing
FRP	Fiber-reinforced plastic
GFR	Glass fiber reinforced
H20	Hemispherical tup with a diameter of 20 mm
NP	Non perforation
PBA	Physical blowing agent
PET	Polyethylene terephthalate
PLA	Polylactic acid
PP	Polypropylene
SEM	Scanning electron microscope
TFP	Top face perforation

List of symbols

a	Acceleration [m s^{-12}]
ds	Strand diameter [mm]
Df	Filament diameter [mm]
E_{test}	Energy test [J]
F	Force [N]
F_{max}	Maximum force [N]
F_r	Flow rate multiplier
g	Gravity acceleration [m s^{-12}]
L_w	Layer width [mm]
L_h	Layer height [mm]
m	Mass [kg]
m_{avg}	Average mass [kg]
N_d	Nozzle diameter [mm]
P_a	Pressure of absorption [Pa]
t	Time [s]
v	Velocity [m s^{-1}]
S	Dimension of the cell in the infill [mm]
S_N	Nozzle speed [mm s^{-1}]
S_e	Extrusion speed [mm min^{-1}]
SEA_ρ	Specific energy absorption to density [J m^3 kg^{-1}]
SEA_m	Specific energy absorption to mass [J kg^{-1}]

t_a	Time of absorption [s]
t_d	Time of desorption [s]
T_a	Temperature of absorption [°C]
T_e	Temperature of extrusion [°C]
TEA	Total energy absorption [J]

Greek letters

δ	Displacement [m]
$\delta_{F_{max}}$	Displacement at maximum force [m]
ρ	Density [kg m^{-3}]
ρ_{avg}	Average density [kg m^{-3}]
ρ_{std}	Density standard deviation [kg m^{-3}]

1 Introduction

Polymeric materials, especially in cellular forms, are increasingly being used in various industries, including biomedical, engineering, aerospace, and sports. These materials are valued for their lightweight properties, structural integrity, and energy absorption capacities, which are influenced by their cellular morphology, such as pore sizes, orientations, and densities [1, 2]. Nature provides a unique example of the strategic use of cellular structures, showing how materials such as the intricate honeycombs of bees or the robust shells of echinoids can achieve exceptional performance through meticulous design [3, 4].

Polylactic acid (PLA) stands out as a benchmark material in the field of sustainable polymers due to its renewable origin and inherent biodegradable properties. Derived from biobased sources such as corn, sugarcane, or beet, PLA significantly reduces reliance on fossil resources, contributing to lower greenhouse gas emissions during its production process [5, 6]. Unlike traditional petroleum-based plastics, the end-of-life phase of PLA showcases its sustainability. Under industrial composting conditions, PLA can decompose into water, carbon dioxide, and biomass, leaving no persistent or toxic residues in the environment [7]. Furthermore, advancements in its mechanical and thermal properties, combined with its competitive cost, make PLA a viable alternative for diverse applications while supporting the principles of a circular economy.

The advent of additive manufacturing (AM) has significantly changed the landscape of materials design and production. AM technologies, including Foam Additive Manufacturing (FAM), have made it possible to create complex and customized parts that utilize cellular structures to enhance mechanical properties. This includes improved strength-to-density ratios and tailored material behaviour [8, 9].Despite these advancements, achieving precise control over the mechanical properties of foam structures through additive manufacturing (AM) remains a challenging effort, primarily due to limitations in machine resolution and the unique complexity of foam properties [10–12].

Foam Additive Manufacturing (FAM) contributes to sustainability by minimizing material waste through its layer-by-layer approach and reducing energy and resource consumption by eliminating molds and tooling. Its monomaterial design simplifies recycling, while the use of CO_2 as a physical blowing agent preserves polymer recyclability, avoiding toxic byproducts. These features position FAM as a sustainable manufacturing process aligned with greener industrial practices [13, 14].

Recent advancements in additive manufacturing have introduced techniques such as direct foam writing and lithographic 3D printing. These technologies offer the potential to design parts with customised foam morphologies, enabling a new level of material optimisation. Foam Additive Manufacturing has emerged as a groundbreaking approach, allowing for the direct integration of foaming processes into 3D printing [15–19]. This technique preserves the chemical integrity of the polymer and facilitates easier recycling processes, making it a sustainable material solution. The research of polymeric foams, particularly PLA (polylactic acid), is gaining traction in the field of sustainable manufacturing and design due to its exceptional balance of mechanical properties and biodegradability. PLA is an ideal candidate for eco-friendly applications, ranging from innovative packaging solutions to the fabrication of advanced composite materials such as Carbon Fiber Reinforced Polymers (CFRP) [20] and Fiber-Reinforced Plastic (FRP). Gomez et al. [21] studied the impact behaviour of sandwich panels with two different sustainable core materials (agglomerated cork and PET foam) reinforced by CFRP laminate. Oliveira et al. [22] present a thorough review of bio-based/green sandwich structures, highlighting the importance of polymer-matrix composites, natural fibres, and thermoplastic resins in developing structures with superior stiffness-to-weight ratios. Niu et al. investigated the influence of different reinforcement types and process parameters on the mechanical properties of PLA, with an emphasis on tensile toughness, identifying specific reinforcement mechanisms for each type of interlayer [23]. They also underscore the potential of PLA in this domain. In addition, Rojas, Scaffaro and Wang [24–26] explore the biodegradability of PLA foams developed for packaging, highlighting their negligible impact on food safety and their resistance to various chemical agents, presenting PLA as a sustainable option for food packaging. Explored the biodegradability of PLA foams developed for packaging, highlighting their negligible impact on food safety and their resistance to various chemical agents, presenting PLA as a sustainable option for food packaging. Although there are promising applications, the use of additive manufacturing techniques to create sandwich structures with homogeneous polymeric cores has been relatively underexplored. Grünewald et al. [27] discussed the challenges and opportunities of using polypropylene (PP) and polyethylene terephthalate (PET) foams in manufacturing such structures, and suggested the need for innovation in using PLA for similar purposes. Alcock et al. [28] studied all-polypropylene composites for sandwich structures, suggesting potential pathways for adopting PLA in similar applications. Brischetto et al. [29] presented an investigation into the mechanical performance of fully PLA honeycomb sandwich structures, revealing promising results that pave the way for further exploration in PLA-based additive manufacturing. Finally, Palomba et al. [30] researched on low-velocity impact tests on bamboo samples and their use in designing PLA multilayer corrugated sandwich structures provides valuable insights into the structural and mechanical advantages of PLA in impact-resistant applications.

The objective of this research is to investigate the impact resistance of sandwich structures made from a single material, PLA. The structures were fabricated using a fully automated, one-step 3D printing process that employs Foam Additive Manufacturing (FAM) for foam-filled cores and traditional honeycomb infill for comparison. This study aims to investigate the impact behaviour of 3D-printed sandwich structures to gain insights into the role of cellular structure morphology in energy absorption and dissipation during impact events. The findings will contribute to the fundamental understanding of the mechanical properties of 3D-printed foams and highlight the potential of FAM in creating next-generation materials that are high-performing and environmentally sustainable.

2 Materials and methods

2.1 Foam Additive Manufacturing

The FAM process involves two main phases: solubilization and extrusion. During solubilization, a polymeric filament is placed inside a pressure vessel, where a physical blowing agent (PBA) is introduced by carefully controlling the absorption pressure (P_a), absorption temperature (T_a), and absorption time (t_a). This controlled environment allows the PBA to dissolve into the polymer, creating a polymer-PBA solution. Following solubilization, the filament undergoes a desorption phase, where it is stored at ambient conditions for a specific duration (t_d) before it is used for printing. The final phase, extrusion, is illustrated in Fig. 1. During extrusion, the polymer-PBA solution is subjected to a rapid decrease in pressure and an increase in temperature as it passes through the nozzle. This rapid change causes the PBA to expand, resulting in the formation of foam within the polymer. Key parameters in the extrusion phase include the extrusion temperature (T_e), extrusion speed (S_e), and nozzle diameter (N_d).

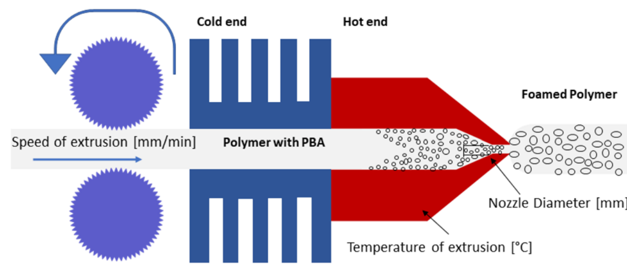

Fig. 1 Extrusion process outline [31]

The advancement of FAM technology offers significant potential for the creation of customised foamed structures with advanced micro- and macro-morphologies. By precisely managing printing parameters, such as absorption pressure and time, desorption time, temperature, and extrusion speed, manufacturers can produce foams with specific, desired characteristics.

In this research, the objective was to validate the AM of thermoplastic polymer foams using a custom-made polylactic acid (PLA) filament. Specifically, PLA 710 grade M microbeads, sourced from Bewi Synbra, were selected to control the thermal history and rheology of the filament. The filaments were produced by the 3D printing filament manufacturer Eumaker in Italy. The PBA used in this study was CO_2.

2.2 Design of the specimens

The specimens, which measured 60x60x20 mm, were 3D printed and subsequently prepared for low-velocity impact testing, according to the standard ISO 6603-2 [32]. The study included eight different specimen types: four with a foamed PLA core, labeled as $F1$, $F2$, $F3$ (F series), and GRAD, and four with a conventional infill core made of un-foamed Bulk PLA (B series), labeled as $B10$, $B40$, $B60$, and $B100$. The images at the bottom of Fig. 2 depict the external surfaces of the specimens from the "F" and "GRAD" series, where the lamination sequence can be observed. This sequence includes 1 mm top and bottom layers with foamed cores of varying densities. At the top of Fig. 2, scanning electron microscope (SEM) images illustrate the cross-sections of the strands that form the specimens, produced using the same parameters as the specimen infill. Specifically, the Bulk strand is highlighted in blue characterized by density $\rho = 1.24\text{g mm}^{-}3$ and strand diameter $d_s = 0.69\text{mm}$, the High-Density foam strand in yellow characterized by $\rho = 0.73\text{g mm}^{-}3$ and $d_s = 1.22\text{mm}$, the Medium Density foam strand in red characterized by $\rho = 0.49\text{g mm}^{-}3$ and $d_s = 1.53\text{mm}$, and the Low-Density foam strand in green characterized by $\rho = 0.23\text{g mm}^{-}3$ and

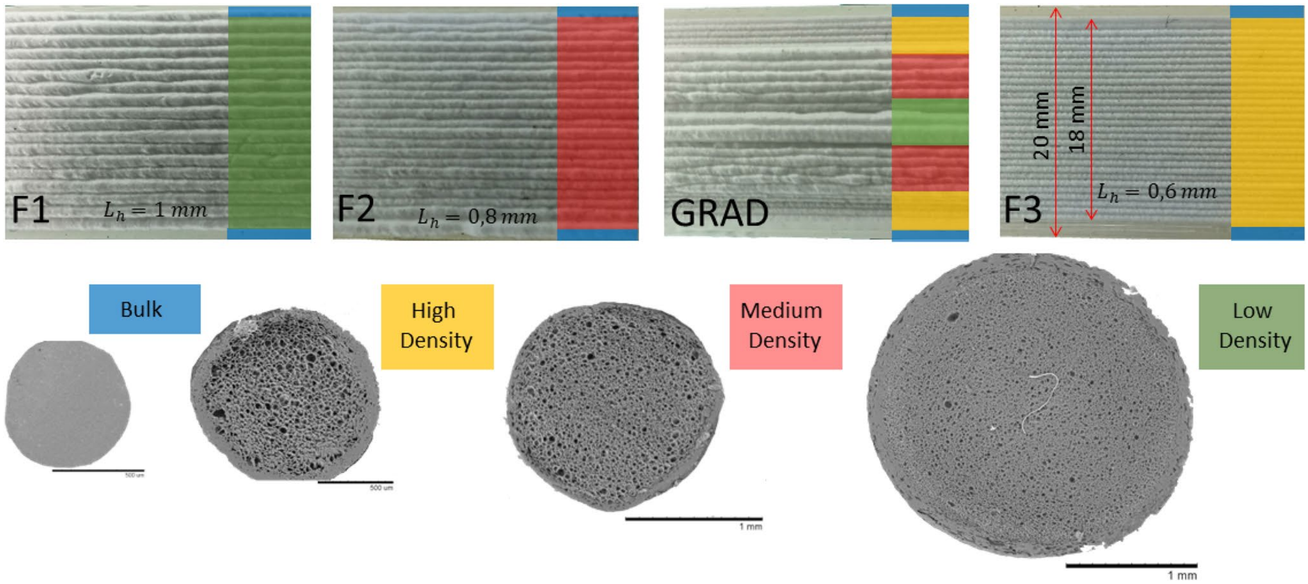

Fig. 2 SEM pictures of the section of the Sandwich structures with a zoom of cross section of a strand realised with the same parameter of the foam

$d_s = 2.31$mm. The lamination sequence for each foamed specimen (F and GRAD series) in the Z direction includes:

Bottom plies made of 1*mm* thickness unfoamed Bulk PLA the create the rigid skin, in Blue for all the specimens.

Core made of 18*mm* thickness with a 100% ±90° foamed infill.

- The *F*3 core with a High-density foam.
- The *F*2 core with a Medium-density foam.
- The *F*1 core with a Low-density foam.
- The *GRAD* specimen with a symmetric lamination sequence that involves all three density foam. The lamination sequence is explicated in Table 2.

Top plies made of 1*mm* of unfoamed Bulk PLA for the top rigid skin.

The *B* series specimens, as depicted in Fig. 3, are constructed using bulk polymer with a honeycomb infill designed to achieve densities similar to their counterparts in the *F* series. It was determined that the three foam densities result in total weights for the specimens comparable to those made with 10%, 40%, and 60% honeycomb infill.

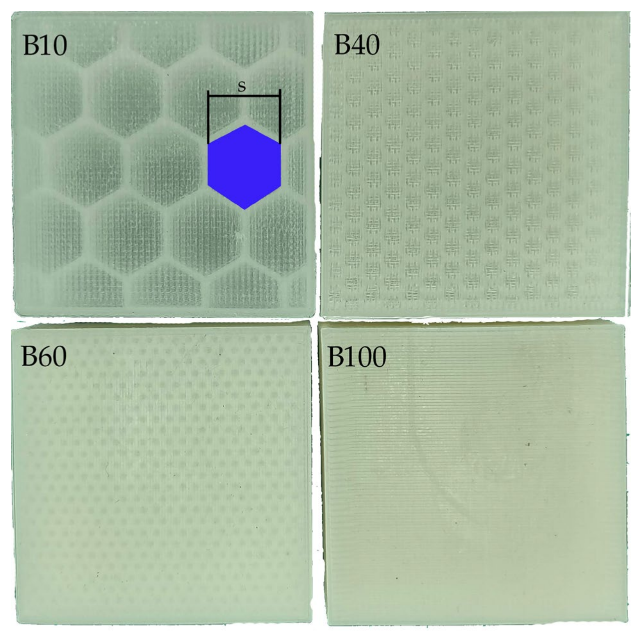

Fig. 3 Overview of bulk specimens showcasing the variation in honeycomb infill patterns. The sequence is arranged from top to bottom, starting with B10, B40, B60 and B100

The lamination sequence for each unfoamed specimen (*B* series) in the Z direction includes:

Bottom plies made of 1*mm* thickness unfoamed Bulk PLA the create the rigid skin.

Core made of 18*mm* thickness with a different percentage of honeycomb infill, as shown in the Table 1.

Top plies 1*mm* of unfoamed Bulk PLA for the top rigid skin.

To test the properties of the chosen PLA, a bulk specimen with 100% linear infill was produced referred as the B100.

2.3 Specimen manufacturing

All the specimens were produced using a fully automated 3D printing process. The process utilised a custom-made filament 3D printer, known as Step 2.1, which is equipped with a commercial hot end, the Vulcano from E3D, featuring a 0.6 mm nozzle. The solubilization parameters (P_a, t_a, t_d) and the extrusion temperature were maintained consistently across all specimens to ensure minimal alteration to the polymer's thermal history. Specifically, the parameters were: $P_a = 40\,bar$, $t_a = 48\,hours$, $t_d = 6\,to\,24\,hours$, and $T_e = 180\,°C$.

Table 1 outlines the essential printing parameters used for creating the various zones of the specimen. These parameters were configured in the slicing software Simplify 3D to produce the G-CODE file, which provides the machine instructions for each specimen.

S_N Refers to the Nozzle Speed, set as the constant speed of the hot end in space. Despite high acceleration settings ($a = 4000mm/s^2$), accelerations are mostly negligible, ensuring a nearly constant speed throughout the process.

L_w Refers to the imposed layer width, which needs to be a multiple of the desired total width of the specimen.

L_h Refers to the imposed layer height, required to be a multiple of the desired total height of the specimen [33].

F_r Refers to the Flowrate Multiplier, a coefficient used to adjust the calculated flowrate to account for die swell [34].

Infill Refers to the internal geometry of the printed part, expressed in terms of percentage and shape.

S Refers to the dimensional measure of the honeycomb cell in the infill of the BULK specimen.

S_e Refers to the imposed extrusion speed, defined as the filament speed in millimeters per minute. This speed is calculated differently from the printing speed, as it is determined by the need to deposit the total volume of the strand, taking into account L_w and L_h. It can

Table 1 Printing parameter, ND*=Not defined

Type	S_N mms^{-1}	S_e $mmmin^{-1}$	L_w mm	L_h mm	F_r %	Infill %	Infill (Angle °)	S mm
F1	100	498.9	1	1	20	100	±90	ND*
F2	60	383.2	0.8	0.8	40	100	±90	ND*
F3	40	215.5	0.6	0.6	60	100	±90	ND*
B10	100	299.3	0.6	0.2	100	10	±120	15
B40	100	299.3	0.6	0.2	100	35	±120	3.3
B60	100	299.3	0.6	0.2	100	60	±120	1.5
B100	100	299.3	0.6	0.2	100	100	±90	ND*

Table 2 Lamination sequence and printing parameter of the gradient specimen

Type	Layer	S_N (mm s^{-1})	S_e (mm min^{-1})	L_w (mm)	L_h (mm)	F_r (%)	t_z (mm)
Bulk	0–5	100	299,3	0,6	0,2	100	1
HighDensity	6–11	40	215,5	0,6	0,6	60	3
MediumDensity	12–17	60	383,2	0,8	0,8	40	4
LowDensity	18–22	100	498,9	1	1	20	4
MediumDensity	23–28	60	383,2	0,8	0,8	40	4
HighDensity	29–34	40	215,5	0,6	0,6	60	3
Bulk	35–40	100	299,3	0,6	0,2	100	1

be computed using Eq. 1, under the assumptions of incompressibility of the polymer melt and conservation of mass.

$$S_e = \frac{L_w \cdot L_h \cdot S_n}{\pi \cdot \left(\frac{Df}{2}\right)^2} \cdot 60 \cdot \frac{F_r}{100} \tag{1}$$

where D_f represents the filament diameter.

The rigid top and bottom layers of all specimens were produced using the same parameters as the $B100$ reference specimen, with detailed printing parameters listed in Table 1.

Table 3 provides a summary of the overall specimen characteristics, including measured mass (m_{avg}), average density (ρ_{avg}), and density standard deviation (ρ_{std}) for the specimens under analysis. As intended, the densities of specimens $B10$ and $F1$, $B40$ and $F2$, and $B60$ and $F3$ are observed to be very similar.

2.4 Experimental set-up

The low-velocity impact tests were carried out by CEAST FRACTOVIS drop test machine (Fig. 4), built in conformity with ISO 6603-2 [32]. This machine allows adjustment of the impactor mass system and the drop height. The machine is equipped with a braking system to avoid multiple impacts. To perform high energy values tests, a springs system can be activated to increase the system energy capacity. The impactor, equipped with a threaded connection, allows interchangeable tups to adapt to different applications. The tup used for the low-velocity impact test campaign is a hemispherical tup (as per "ISO 6630") with a diameter equal to 20 mm (H20). The tests were conducted using an impact mass, kept constant, of 6.5 kg. The specimens were supported by a cylindrical support with an internal diameter of 40 mm and an external diameter of 90 mm. To quantify the energy absorption properties, the following parameters were evaluated:

- Total energy absorption [J]

$$TEA = \int_0^{\delta_{max}} F\delta \tag{2}$$

where: F represent the force and δ the displacement.

- Specific energy absorption relative to mass [J/kg]

$$SEA_m = \frac{TEA}{m} \tag{3}$$

- Specific energy absorption relative to density [J*m^3/kg]

Fig. 4 Drop test machine

$$SEA_\rho = \frac{TEA}{\rho} \tag{4}$$

These parameters provide a comprehensive understanding of the material's ability to absorb energy during impact events, normalized by mass and density, making them suitable for comparative analyses with other lightweight structures.

3 Results

Figure 5 reports the front and rear sides of the impacted specimen at 30 J showing the interaction between the impactor and the sample, and the impact damage that is narrowed under the contact point between the specimen and the impactor for the foam and grad samples and more brittle for bulk samples for which the collapse occurred with the breakage in four parts. However, as the impact energy increases above 25 J all the specimen show a perforation of both the faces and the core.

Figure 6 shows the trend of the load–displacement curves of all tested specimen impacted at different energy levels until complete penetration, offering a detailed representation of the specimens mechanical response. Across all examined

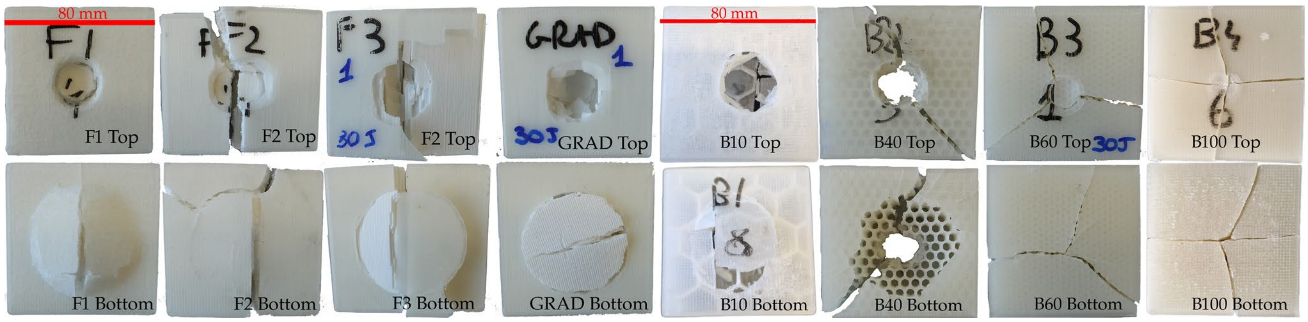

Fig. 5 Foam and bulk specimens after impact test

Table 3 Mass and density values for the different families of specimens

Type	m_{avg} (g)	ρ_{avg} (kg m^{-3})	ρ_{std} (kg m^{-3})
F1	23.66	328.65	7.63
F2	40.34	561.60	4.09
F3	56.96	791.11	14.97
GRAD	41.86	581.34	4.88
B10	24.83	344.90	16.79
B40	42.23	586.49	11.89
B60	57.11	793.19	7.82
B100	90.54	1257.53	2.60

specimen groups, a characteristic force-displacement trend is noticeable, characterized by an initial phase where the load increases linearly with displacement, followed by a peak load attributed to the contact between the tup and the top skin, and finally, a subsequent decrease in load. The type of specimen has a strong effect on the impact force and the duration of the impact.

In particular, comparing the foam and grad structures (Figs. 6 and 8) it is possible to notice an increase in the maximum load of the foam structures going from specimen $F1$ to $F3$, indicating an increasing rigidity upon the impact of the material also indicated by the greater slope of the linear section of the curve. In particular, the first maximum load of about 2000 N is reached for $F1$ specimen while it increases for $F2$ and $F3$ ones and this is certainly justified by the greater density of the latter types of specimens. For all foam structures, the penetration of the specimen is reached for energy between 25 J and 30 J, as indicated in bold in Table 4.

It is worth noting that the first maximum value represents the force that causes the failure of the skin and appears to be unrelated to the impact energy. About the $F3$ samples for all impacted energies, a first change in the linear pendency can be observed at about 1 ms due to the upper skin failure, while several important drops of loads were recorded due to the interaction of the impactor with the core of the sample (Fig. 10). Important knowledge can be acquired from the velocity-time plot, which can show the capacity of the material to decelerate and stop the impacting mass as reported in Fig. 7, which shows the trend of the velocity-time curves for the family of foam specimens.

The low-velocity impact tests performed at the energy of 25 J for the $F1$ specimen induce the total perforation of the specimen, which cannot stop the mass: the velocity decreases without reaching the zero value. The same behaviour is seen for impact energy higher than 25 J for the other specimen types. However, for energy values less than the penetration ones, the $F1$ samples slow down the mass in a range of time greater than the other structures since the more important damage recorded.

Figure 8 shows the force-displacement curves of bulk samples for different impact energies for all fill densities. In this case, for all tested samples, the maximum peak load increases as the impact energy increases. Curves for specimens characterized by low density show a high level of curve noise due to the failure of the core cell walls. These oscillations decrease as the density increases, showing a smoother curve. Also, the maximum load increases with the bulk density. However, the displacement in correspondence of the load peak decreases since the higher density of the specimen also visible in the mode breakage in Fig. 5.

Figure 9 shows the trend of the velocity-time curves for the family of bulk specimens. For low values of impact energy each specimen is able to stop the mass and the deceleration is faster the higher the density of the specimen.

In Table 4 the value of energy test (E_{test}), maximum force ($F_{\max}$), displacement at maximum force ($\delta_{F\max}$), total energy absorbed (TEA) and specific energy absorbed with respect to mass and density (respectively SEA_m and SEA_ρ) are reported and highlight that the best performance in terms of specific energy absorbed is reached on the bulk specimen $B40$. For foamed specimens, the highest value of SEA_ρ is on the $F1$ specimen tested with an energy of 25 J. Comparing the specimen types at the same density highlights that at low densities (in $F1$ and $B10$ specimens) there are similar maximum load values but the displacement at maximum

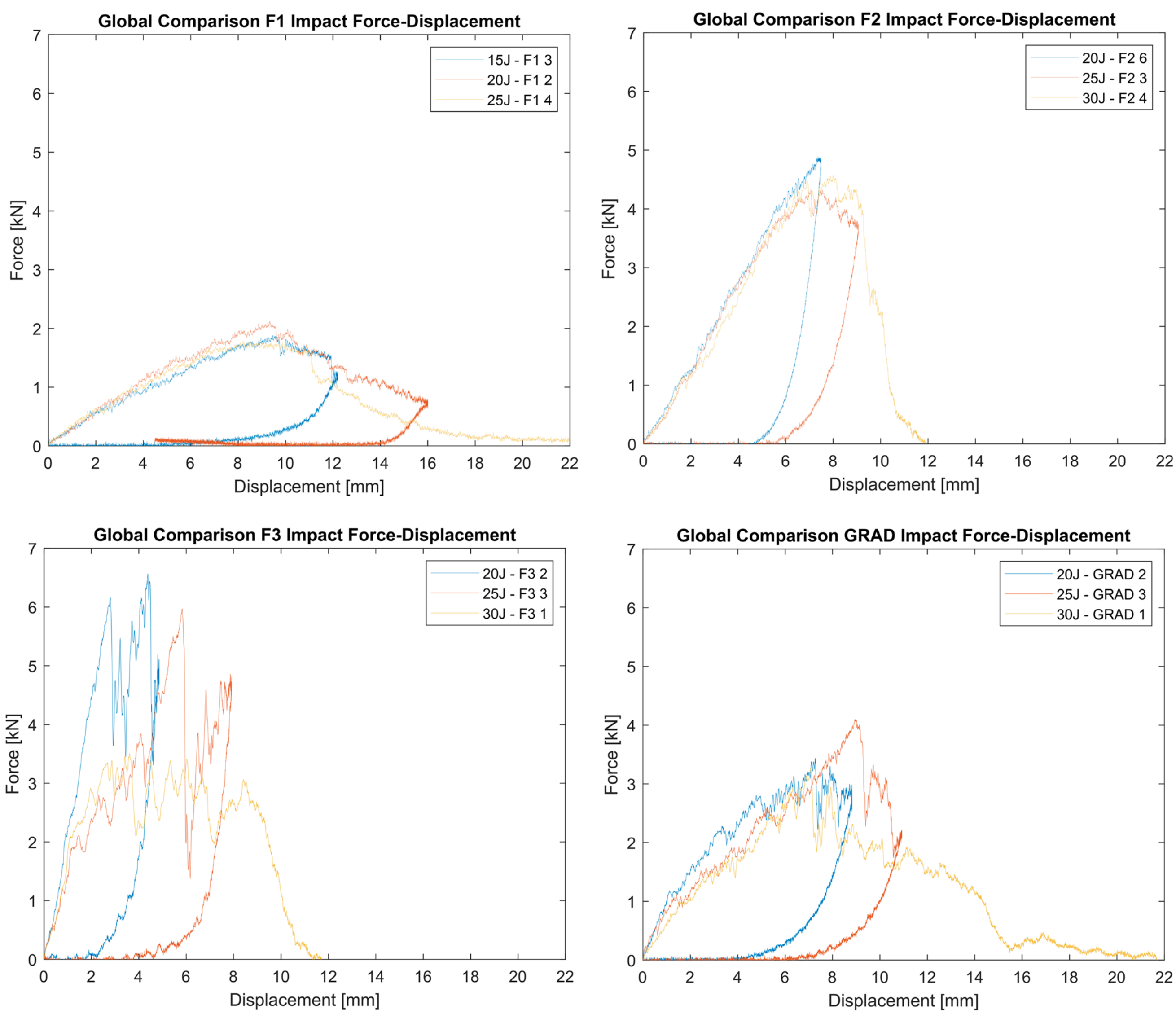

Fig. 6 Foam force-displacement curves

force is greater on the foamed specimens. Higher perforation energies are recorded on the $F1$ specimens. At medium densities (in specimens $F2$, $GRAD$, and $B40$) higher perforation energy and maximum load values are noted on the unfoamed species, but lower displacement values. However, at high densities (in the $F3$ and $B60$ specimens), the same perforation energy and similar values of displacement relative to the maximum force are recorded, but higher peak maximum force for bulk specimens.

4 Discussion

The failure modes of the specimens after the impact tests were analysed by high-resolution optical microscopy. Figure 10 shows the optical images and scanning electron microscopy of the section of the foamed specimens section; Fig. 11 refers to the bulk specimens. The morphology of the foam core was observed before and after the tests, which allowed us to explain the load vs. displacement curves. The $F1$ specimens experienced a clear foam cell collapse, which is the mechanism allowing the energy absorption of these specimens. The same behaviour can be seen for the $F2$ specimens, whose higher density gives a lower size of the pores. The global failure of the $F1$ and $F2$ specimens is dominated by upper skin indentation, core densification and out-of-plane displacement of the bottom skin. The intralaminar cracks of the core has the typical pine-tree pattern of thick laminates [35]. The ability to give out of plane displacements generally characterizes a sctructure prone to energy adsorption [36]. The $F3$ specimens experienced a different failure mode, where the

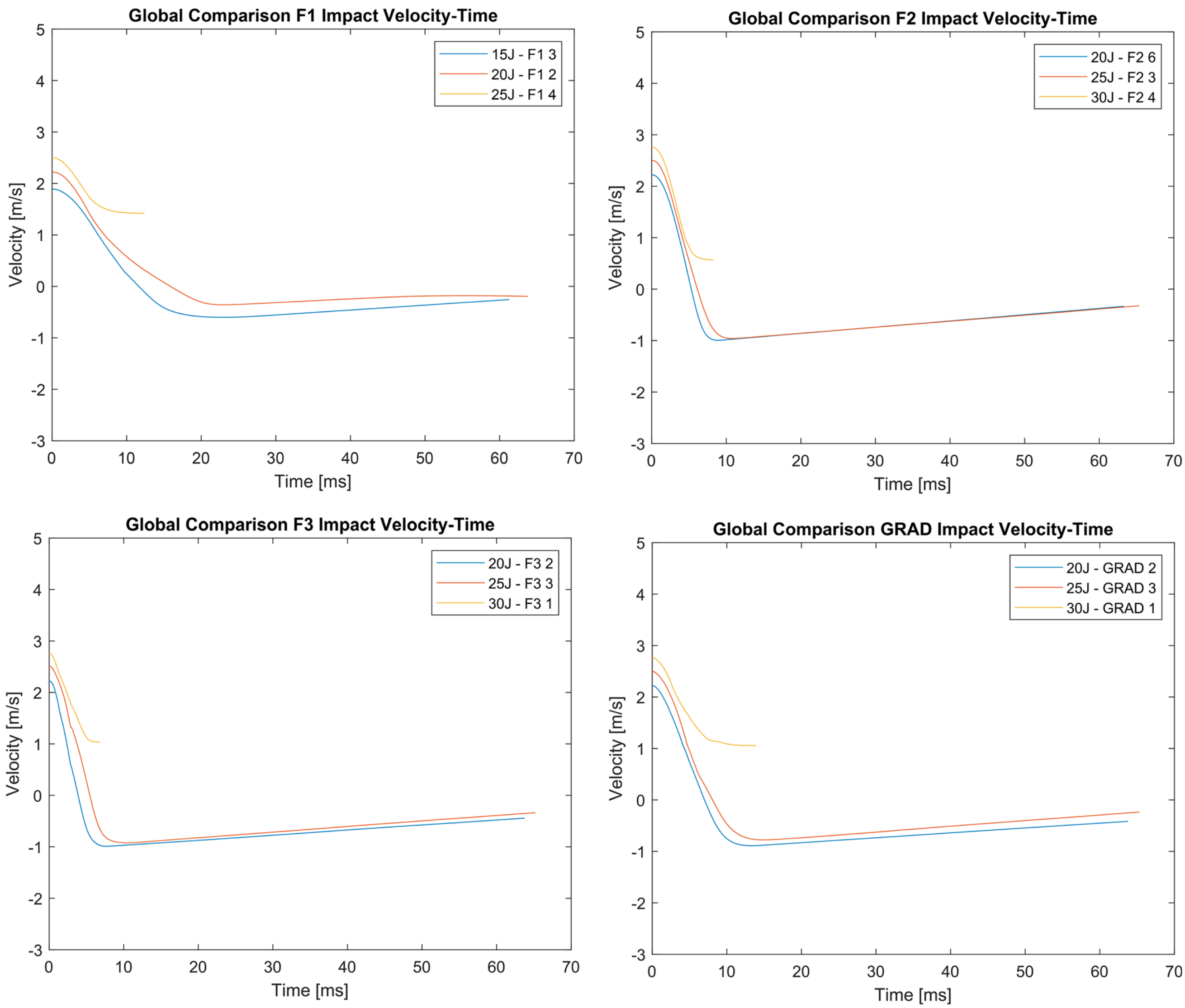

Fig. 7 Foam velocity-time curves

interlayer debonding mainly occurred. The out-of-plane displacement and the indentation are very limited. Due to the higher stiffness of the specimen, the inability to bend caused the breakage of the layers bonding. Moreover, at higher optical magnitude, the failure mechanism of the core highlights that the densification didn't occur as in the $F1$ and $F2$ typologies. The progressive interlayer bonding failure is also visible in the force vs. displacement curve, where a number of load drops was recorded during the impact tests.

In Fig. 11 the B10 the failure of B10 specimens is characterised by the fracture of the honeycomb cell walls. The corresponding micrograph (B10a) highlights the delamination of the layers. In contrast, for the specimens B40a, B60a, and B100a, the reduced cell size (S) inhibits delamination. Instead, horizontal crack propagation is observed, highlighting a distinct failure mechanism compared to the lower-density specimens.

By analysing the force-displacement curves, the average value of the slope in the linear region was extracted. Figure 12 illustrates how the greater stiffness of the material is found in the $F3$ family specimens, followed by the F2 and GRAD families, where the value of the angular coefficient is quite similar. Finally, in the $F1$ family specimens, this value is low due to the lower density.

Table 5 shows the peak acceleration of the specimens, at the energy value that causes total perforation. The values recorded during the impact tests highlights that the tested specimens can be employed as cushioning materials to reduce the impact damage, for example, during the harvesting in agriculture [37]. By cross-reading the peak accelerations, the peak loads, the impact duration, which represents

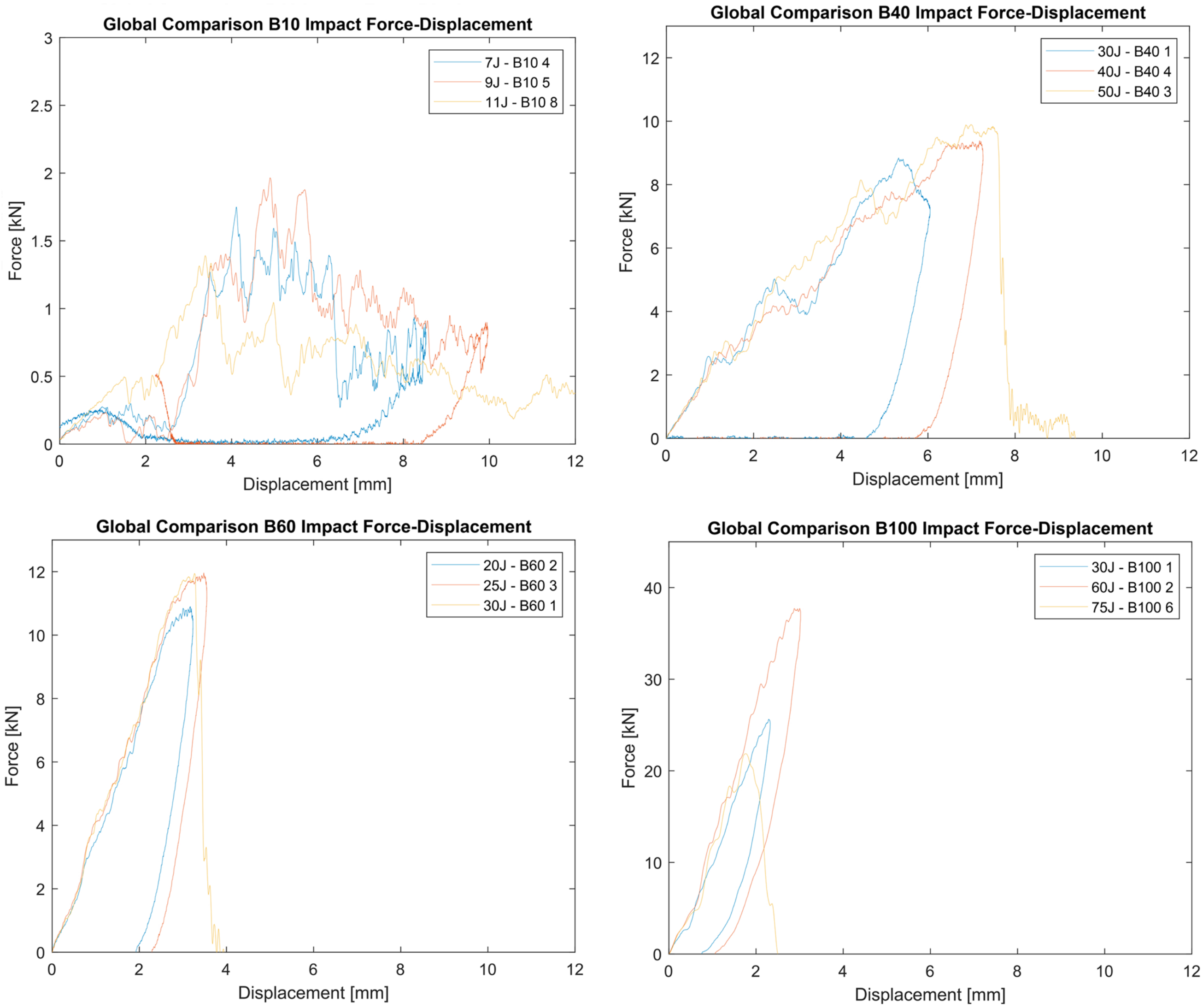

Fig. 8 Bulk force-displacement curves

the time during which the transfer of energy takes places during the impact, and the ability to deform under the load, $F2$ specimens have good mechanical behaviour [38].

A further interesting property of the analysed specimens is observed in Fig. 13, where the specific adsorbed energy referred to the density reported. By considering the overall results obtained from the impact tests as well as the failure modes, the $F2$ typology shows a SEA_{ρ} value near other sandwich structures analysed in [39]. Due to the nature of the parent material, the value are below to multilayers trapezoidal corrugated and honeycomb aluminum sandwich structures, but similar to sandwich structures with plywood core and both GFR and CFR skins (Table 6).

Figure 14 shows the trend of the loads (solid line curves) and energies (dashed line curves), as a function of the displacement, of the specimens tested at an energy level close to that which caused their failure. The initial slope changes in the energy-displacement curves of the foam specimens can be attributed to the failure of the upper skin (about 1 mm displacement). Subsequently, multiple changes were registered due to the interaction of the impactor with the sample core. Similar behavior is also recorded on the bulk specimens $B10$, $B40$, and $B60$ with an initial change in the slope of the energy-displacement curve due to upper skin failure subsequent changes due to core failure. On the $B100$ sample an initial slope change is shown followed by a linear trend of the energy-displacement curve.

Figure 15 shows the force-displacement curves of the impact tests at the energy that causes the total perforation of the specimens. It can be observed that for foamed specimens F1 and GRAD, the striker is able to fully penetrate the specimens. For specimens F2 and F3 the striker only reaches

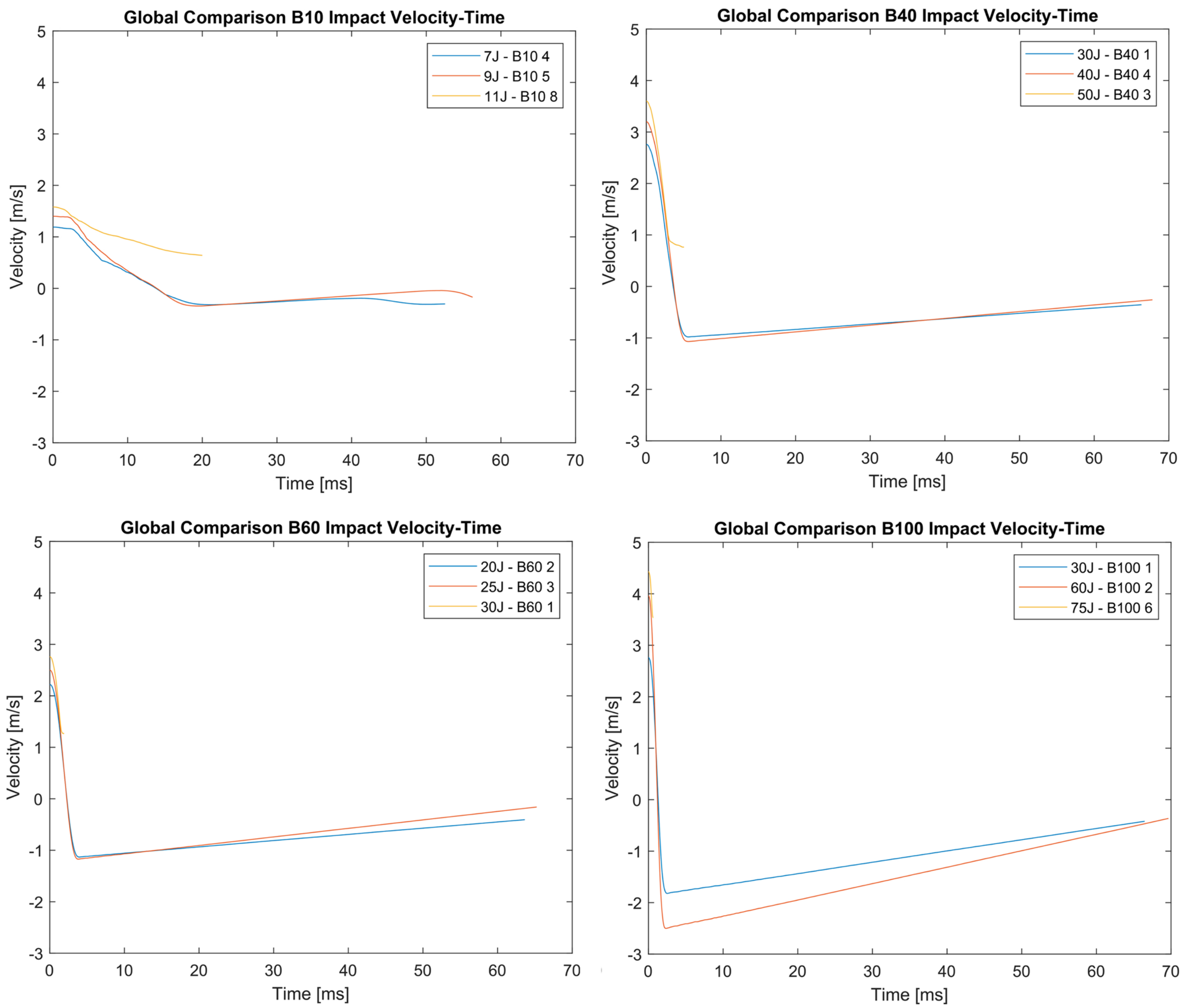

Fig. 9 Bulk velocity-time curves

half the height of the specimens. Comparing the results with the unfoamed bulk specimens, it is evident that the observed displacement values are higher for the foam types.

A failure map mode is shown in Fig. 16, allowing the failure mechanisms to be analysed and visualised as a function of specimens' density and impact energy. The diamond, circle and square markers indicate non-perforation of the specimen (NP), top face perforation (TFP) and total perforation of the specimen (TPF + TFP), respectively. These markers allow the specimens' behaviour under different impact loading conditions to be identified and graphically compared. For comparison purposes, the full marker indicates the bulk typology and the empty marker indicates the foam one. In the low-density plot area, the comparison between the two typologies shows that the energy required for the total perforation of the foam *F*1 specimen is 127% higher than for the bulk *B*10. In the medium density zone, it is highlighted that foam *F*2 and *GRAD* gradient specimens require almost the same energies for both specimen's upper skin and total perforation. In this case, the perforation energy of the bulk *B*40 sample is 67% higher. The total perforation of the foam and bulk specimens, *F*3 and B60, in the high-density zone occurs with the same energy value (30 J). It can also be empathised that the bulk type experienced extremely brittle behaviour with respect to foam from non-perforation to total perforation of the specimen (the same behaviour occurs on the *B*100 bulk specimens). In the design phase of a component, the use of the failure mode map allows the selection of the most suitable material according to

Table 4 Low-velocity impact test results

Type	Test N°	E_{test} (J)	F_{max} (N)	δ_{max} (mm)	TEA (J)	SEA_m (J kg^{-1})	SEA_ρ (J m^{3}kg^{-1})
F1	3	15	1.89	9.47	12.43	526.31	0.04
	2	20	2.12	9.33	18.67	763.63	0.05
	4	**25**	**1.79**	**8.21**	**19.57**	**838.58**	**0.06**
F2	6	20	4.89	7.36	15.76	385.47	0.03
	3	25	4.33	7.06	20.88	519.28	0.04
	4	**30**	**4.57**	**7.99**	**28.22**	**702.60**	**0.05**
F3	2	20	6.57	4.38	14.94	256.70	0.02
	3	25	5.97	5.83	20.98	373.38	0.03
	1	**30**	**3.51**	**3.61**	**25.37**	**449.01**	**0.03**
GRAD	2	20	3.44	7.28	15.75	378.96	0.03
	3	25	4.10	8.94	21.85	517.33	0.04
	1	**30**	**3.28**	**7.08**	**25.98**	**621.80**	**0.04**
B10	4	7	1.80	4.12	4.88	198.71	0.01
	5	9	2.00	4.89	7.40	308.24	0.02
	8	**11**	**1.44**	**3.40**	**9.57**	**379.32**	**0.03**
B40	1	30	8.84	5.33	25.45	599.89	0.04
	4	40	9.39	7.19	35.53	849.80	0.06
	3	**50**	**9.89**	**6.98**	**47.11**	**1087.15**	**0.08**
B60	2	20	10.90	3.17	13.81	244.61	0.02
	3	25	11.96	3.48	18.45	321.07	0.02
	1	**30**	**11.94**	**3.27**	**22.80**	**397.33**	**0.03**
B100	1	30	25.63	2.29	16.18	178.83	0.01
	2	60	37.72	2.88	35.44	392.32	0.03
	6	**75**	**22.87**	**1.77**	**26.92**	**295.33**	**0.02**

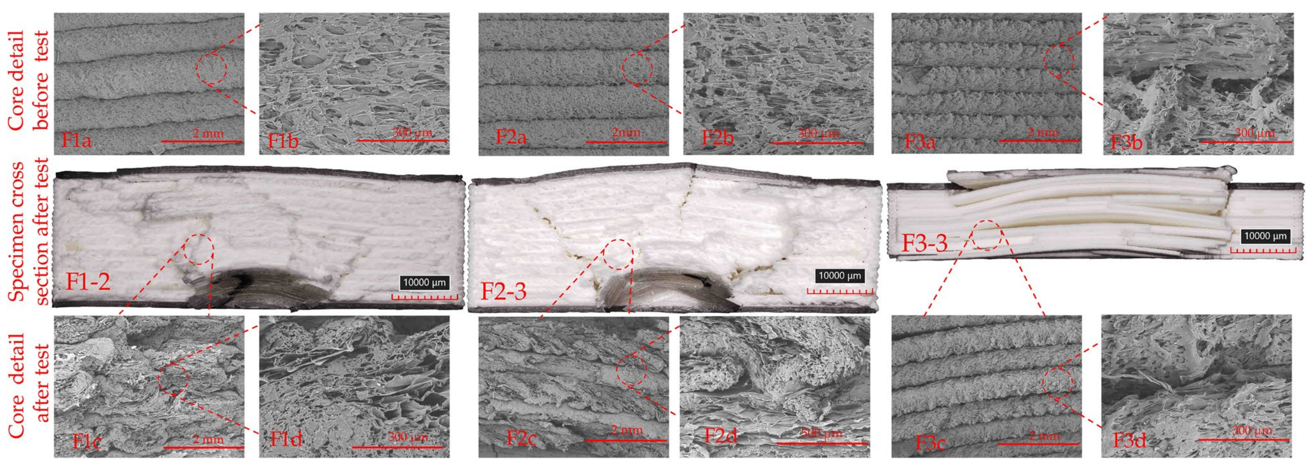

Fig. 10 Optical and scanning electron microscopies of the section of the foam sandwich structures after impact test

certain operating conditions. By comparing the different impact behaviour of the analysed structures in relation to density and impact energy, this chart provides useful indications for optimising component performance and reliability.

4.1 Sustainability and Industrial Applications of FAM

The ability of Foam Additive Manufacturing to create tailored monomaterial structures on demand, with precise

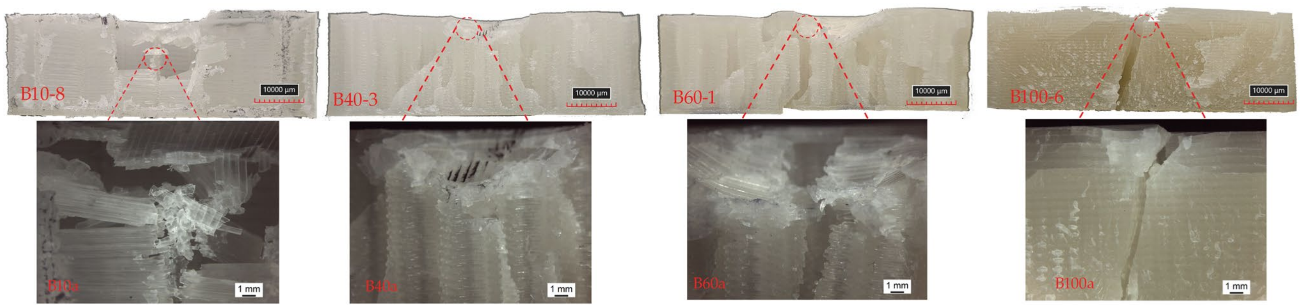

Fig. 11 Visual inspection and microscopic images of the bulk specimens section after impact test

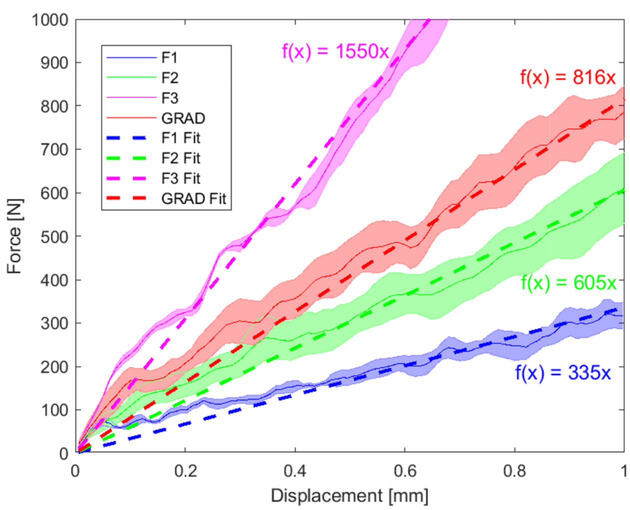

Fig. 12 Force-displacement curves for each foam specimen. The shaded error bars indicate the standard deviation calculated on each repetition

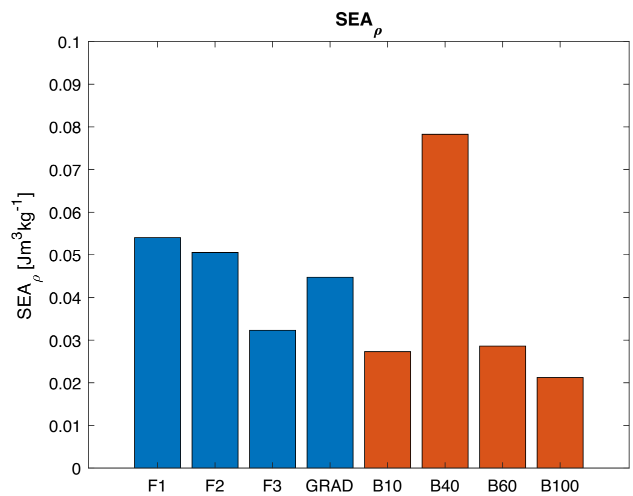

Fig. 13 Specific energy absorbed comparison

Table 5 Slope of the Force vs. Displacement curves, which represents a measure of the specimens' stiffness

Type	*Slope* (Nmm^{-1})
F1	335
F2	605
F3	1550
GRAD	816

Table 6 Peak acceleration value for each specimen type

Type	*a* (ms^{-12})	Type	*a* (ms^{-12})
F1	288	B10	272
F2	589	B40	128
F3	811	B60	163
GRAD	557	B100	513

control over foam morphology, is a key advantage demonstrated in this study and supported by recent findings [40]. This capability enables the production of lightweight structures with density gradients and customized properties, opening new opportunities for high-performance, sustainable solutions across diverse industries.

In the automotive sector, FAM-produced foams can be utilized in crash absorbers, interior panels, and energy-dissipating systems. These lightweight components not only improve fuel efficiency but also enhance safety through superior impact resistance. Additionally, the design flexibility of FAM allows for the integration of tailored density zones, optimizing performance under specific loading conditions.

The aerospace industry can leverage the strength-to-weight ratio of FAM materials for energy-absorbing layers, thermal insulation, and non-load-bearing interior components. The ability to produce monomaterial structures simplifies recycling and supports the sector's sustainability goals by reducing both the environmental impact and the weight of aircraft components.

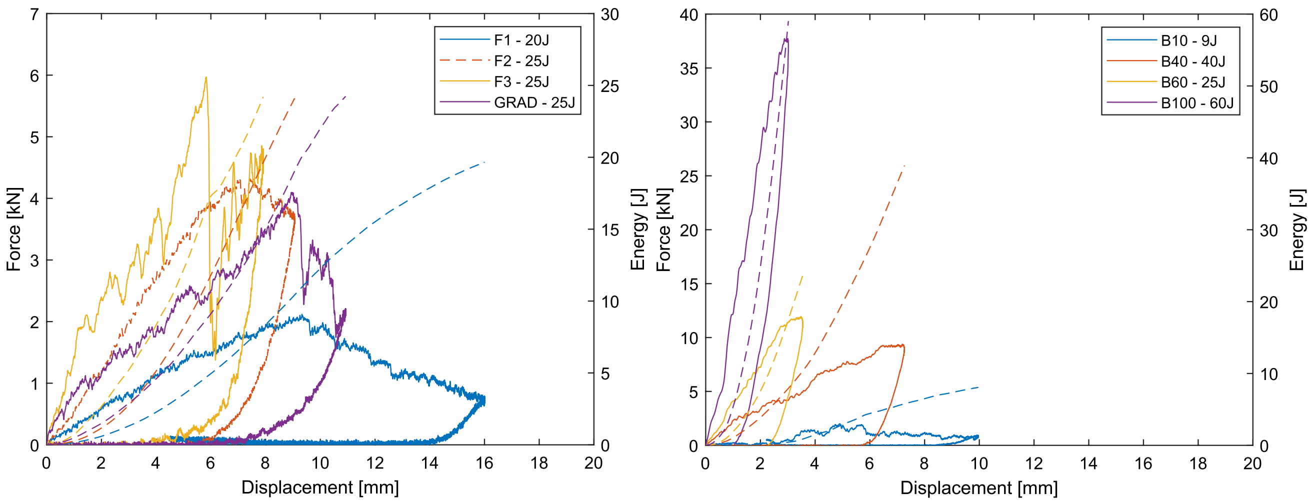

Fig. 14 Force-energy-displacement curves at lower perforation energy

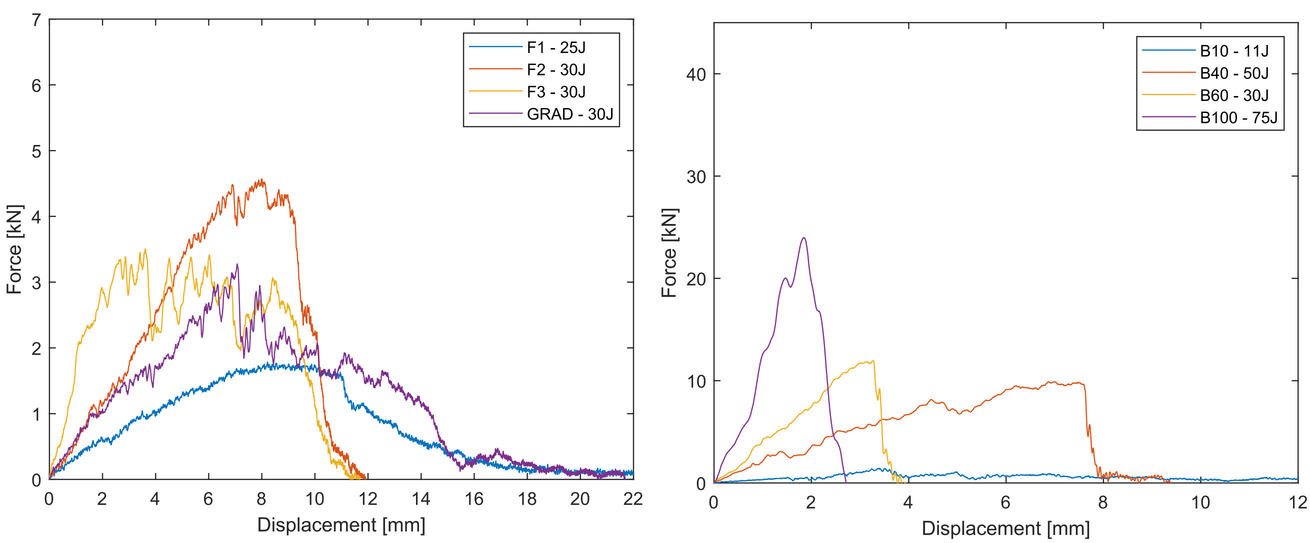

Fig. 15 Comparison of force-displacement curves for foam (left) and bulk (right) specimens at perforation energies

In construction, FAM foams offer innovative solutions for thermal and acoustic insulation. The ability to control foam morphology enables the creation of materials with superior insulating properties and tailored performance, providing effective alternatives to traditional, less environmentally friendly building materials.

Moreover, filtration systems and food packaging represent emerging areas of application for PLA-based foams. In filtration, the control over foam porosity allows for the development of effective filters for air and liquid purification. In food packaging, FAM enables the production of biodegradable, recyclable materials that can be further enhanced with nanotechnologies to improve barrier properties and extend shelf life [41, 42].

The integration of recycled polymers and the use of physical blowing agents like CO_2 further highlight FAM's alignment with circular economy principles. By combining high performance with sustainability, FAM positions itself as a transformative technology capable of addressing critical challenges in automotive, aerospace, construction, and packaging industries, paving the way for greener and more efficient manufacturing practices.

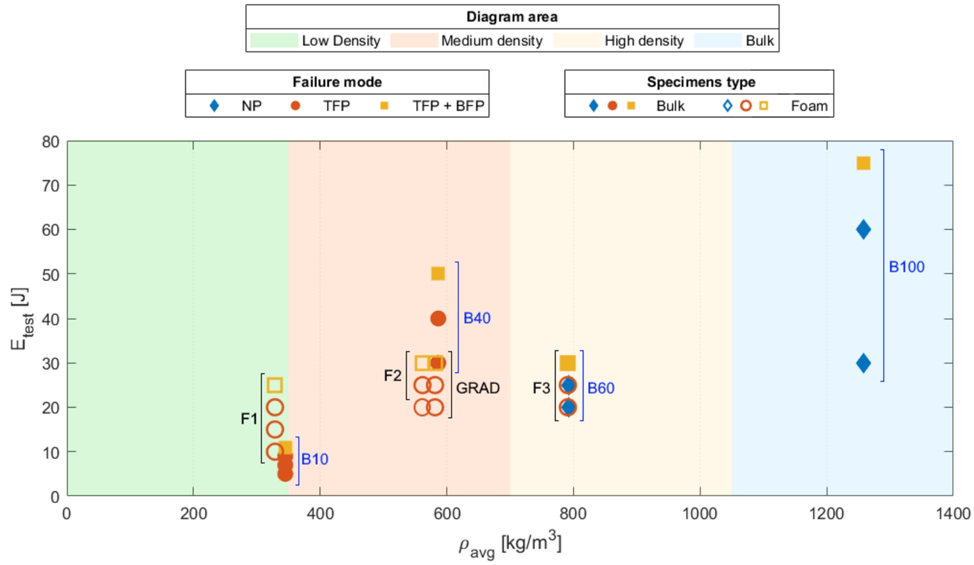

Fig. 16 Failure map comparison in the Energy-Density plane for the different type of specimen

5 Conclusion

This research explored the energy absorption properties and failure mechanisms of mono-material sandwich structures made of the Foam Additive Manufacturing process under low-velocity impact events. The analyses revealed that foamed structures exhibit remarkable impact strength, with significant differences in energy absorption behaviour compared to structures with traditional honeycomb filling. From the failure mode map considering impact energy vs. density, it is evident that the performance of foamed specimens, particularly the F1 type, is superior to bulk specimens of similar density. The brittle failure of the bulk specimens highlights that the F2 foam specimens, despite having lower perforation energies, experience higher displacements and, consequently, maintain some residual performance without brittle failure. Similar observations can be made for the F3 foam type. High-resolution optical microscopy showed that the foam specimens have significant displacements due to core indentation. This behaviour is also highlighted by evaluating the stiffness of the foam specimens. These results contribute to understand the mechanical impact properties of 3D-printed mono-material sandwich structures and underline the potential of FAM in the design of innovative materials that are both high-performance and environmentally sustainable.

The FAM process not only enhances mechanical properties but also embodies principles of sustainable manufacturing. Its material efficiency reduces waste, and the integration of foaming with additive manufacturing avoids the use of harmful chemical agents, preserving the recyclability of the material. These features align with broader environmental goals, supporting the development of low-impact manufacturing systems. Future work could explore energy consumption comparisons between traditional and FAM methods to further quantify its ecological benefits [43].

Furthermore, the design of this type of mono-material foam, printed using additive manufacturing techniques, allows for the creation of specific geometries that are compostable, recyclable, and low-cost for applications in food packaging. This suggests that the adoption of FAM could lead to specific innovations in the design of materials requiring high impact resistance, paving the way for future developments in the research of sustainable and high-performance materials across various industrial applications.

Acknowledgement We acknowledge financial support under the National Recovery and Resilience Plan (NRRP), Mission 4, Component 2, Investment 1.1, Call for tender No. 104 published on 2.2.2022 by the Italian Ministry of University and Research (MUR), funded by the European Union – NextGenerationEU– Project Title 3D Famil– CUP E53D23003240006 - Grant Assignment Decree No. 742 adopted on 30/5/23 by the Italian Ministry of Ministry of University and Research (MUR). This work was supported by the Italian Ministry of Research under the complementary actions to the NRRP "Fir4MedRob - Fit for Medical Robotics" Grant (#PNC0000007).

Funding Open access funding provided by Università degli Studi di Milano within the CRUI-CARE Agreement. Andrea Lorenzo Henri Sergio Detry acknowledges partial support from the EIC project ARCHIBIOFOAM under grant agreement 101161052.

Data availability Data will be made available on request.

Declarations

Conflict of interest The authors declare that they have no known competing financial interests or personal relationships that could have appeared to influence the work reported in this paper.

Open Access This article is licensed under a Creative Commons Attribution 4.0 International License, which permits use, sharing, adaptation, distribution and reproduction in any medium or format, as long as you give appropriate credit to the original author(s) and the source, provide a link to the Creative Commons licence, and indicate if changes were made. The images or other third party material in this article are included in the article's Creative Commons licence, unless indicated otherwise in a credit line to the material. If material is not included in the article's Creative Commons licence and your intended use is not permitted by statutory regulation or exceeds the permitted use, you will need to obtain permission directly from the copyright holder. To view a copy of this licence, visit http://creativecommons.org/licenses/by/4.0/.

References

1. Lee ST *Foam Extrusion: Principles and Practice*. (2000)
2. Ambekar RS, Kushwaha B, Sharma P, Bosia F, Fraldi M, Pugno NM, Tiwary CS (2021) Topologically engineered 3d printed architectures with superior mechanical strength. Materials Today 48:72–94
3. Lakes R (1993) Materials with structural hierarchy. Nature 361(6412):511–515
4. Perricone V, Grun TB, Rendina F, Marmo F, Candia Carnevali MD, Kowalewski M, Facchini A, De Stefano M, Santella L, Langella C, Micheletti A (2022) Hexagonal voronoi pattern detected in the microstructural design of the echinoid skeleton. Journal of The Royal Society Interface 19(193):20220226
5. Sohn YJ, Kim HT, Baritugo KA, Jo SY, Song HK, Park SY, Park SK, Pyo J, Gil H, Kim H, Na J, Park C, Choi JI, Joo JC, Park SJ (2020) "Recent advances in sustainable plastic upcycling and biopolymers," *Biotechnology Journal*, vol. 15
6. Yu X, Liu H, Yan M, Li F, Ke N, Wu G, Chen S, Wang Y (2024) Integration design of toughening agent for poly(lactic acid) with compatibility, transparency, and environmental friendliness. ACS Applied Polymer Materials 6:5555–5565
7. Hottle TA, Bilec MM, Landis AE (2017) Biopolymer production and end of life comparisons using life cycle assessment. Resources, Conservation and Recycling 122:295–306
8. Eren O, Sezer HK, Yalçin N (2022) Effect of lattice design on mechanical response of polyjet additively manufactured cellular structures. Journal of Manufacturing Processes 75:1175–1188
9. Park K-M, Min K-S, Roh Y-S (2022) Design optimization of lattice structures under compression: study of unit cell types and cell arrangements. Materials 15(1):97
10. Visser CW, Amato DN, Mueller J, Lewis JA (2019) Architected polymer foams via direct bubble writing. Advanced Materials 31(46):1904668
11. Wirth DM, Jaquez A, Gandarilla S, Hochberg JD, Church DC, Pokorski JK (2020) Highly expandable foam for lithographic 3d printing. ACS applied materials & interfaces 12(16):19033–19043
12. Lichade KM, Pan Y (2023) Continuous printing of bone-inspired hierarchical porous objects using video projection-based stereolithography. Journal of Manufacturing Processes 107:144–154
13. Gibson I, Rosen DW, Stucker B, Khorasani M, Rosen D, Stucker B, Khorasani M (2021) *Additive manufacturing technologies*, vol. 17. Springer
14. Ngo TD, Kashani A, Imbalzano G, Nguyen KT, Hui D (2018) Additive manufacturing (3d printing): A review of materials, methods, applications and challenges. Composites Part B: Engineering 143:172–196
15. Tammaro D, Detry ALH, Landonfi L, Napolitano F, Villone MM, Maffettone PL, Squillace A (2021) "Bio-lightweight structures by 3d foam printing," in *2021 IEEE 6th International Forum on Research and Technology for Society and Industry (RTSI)*, pp. 47–51, IEEE
16. Landolfi L, Detry A, Tammaro D, Villone M, Maffettone P, Squillace A et al (2023) Additive foam manufacturing. MATERIALS RESEARCH PROCEEDINGS 35:111–117
17. Paquet E, Bernard A, Furet B, Garnier S, Le Loch S (2021) Foam additive manufacturing technology: main characteristics and experiments for hull mold manufacturing. Rapid Prototyping Journal 27(8):1489–1500
18. Cuadra-Rodríguez D, Barroso-Solares S, Rodríguez-Pérez M, Pinto J (2022) Production of cellular polymers without solid outer skins by gas dissolution foaming: A long-sought step towards new applications. Materials & Design 217:110648
19. Nofar M, Utz J, Geis N, Altstädt V, Ruckdäschel H (2022) Foam 3d printing of thermoplastics: a symbiosis of additive manufacturing and foaming technology. Advanced Science 9(11):2105701
20. Yuan B, Ye M, Hu Y, Cheng F, Hu X (2020) Flexure and flexure-after-impact properties of carbon fibre composites interleaved with ultra-thin non-woven aramid fibre veils. Composites Part A: Applied Science and Manufacturing 131:105813
21. Gomez A, Sanchez-Saez S, Barbero E (2023) Experimental analysis of the impact behaviour of sandwich panels with sustainable cores. Composites Part A: Applied Science and Manufacturing 166:107383
22. Oliveira PR, May M, Panzera TH, Hiermaier S (2022) Bio-based/green sandwich structures: A review. Thin-Walled Structures 177:109426
23. Niu G, Tao Y, Zhang R, Feng X, Deng H, Ren M, Sun J, Peijs T (2024) Toughening of self-reinforced pla films using pla nanofiber mats and oriented pla tapes as interlayers. Composites Part A: Applied Science and Manufacturing 185:108267
24. Rojas A, Torres A, López de Dicastillo C, Velásquez E, Villegas C, Faba S, Rivera P, Guarda A, Romero J, Galotto MJ (2022) Foaming with scco2 and impregnation with cinnamaldehyde of pla nanocomposites for food packaging. Processes 10(2)
25. Scaffaro R, Gulino EF, Citarrella MC, Maio A (2022) Green composites based on hedysarum coronarium with outstanding fdm printability and mechanical performance. Polymers 4(6)
26. Wang X, Huang L, Li Y, Wang Y, Lu X, Wei Z, Mo Q, Zhang S, Sheng Y, Huang C, Zhao H, Liu Y (2024) Research progress in polylactic acid processing for 3d printing. Journal of Manufacturing Processes 112:161–178
27. Grünewald J, Parlevliet P, Altstädt V (2017) Manufacturing of thermoplastic composite sandwich structures: A review of literature. Journal of Thermoplastic Composite Materials 30(4):437–464
28. Alcock B, Cabrera N, Barkoula N-M, Peijs T (2006) Low velocity impact performance of recyclable all-polypropylene composites. Composites Science and Technology 66(11):1724–1737
29. Brischetto S, Torre R et al (2020) Honeycomb sandwich specimens made of pla and produced via 3d fdm printing process: An experimental study. Journal of Aircraft and Spacecraft Technology 4(1):54–69
30. Palomba G, Hone T, Taylor D, Crupi V (2020) Bio-inspired protective structures for marine applications. Bioinspiration & Biomimetics 15(5):056016
31. Epasto G, Rizzo D, Landolfi L, Detry ALHS, Papa I, Squillace A (2024) Design of monomaterial sandwich structures made with foam additive manufacturing. Journal of Manufacturing Processes 121:323–332
32. International Organization for Standardization (2000) "Plastics - determination of puncture impact behaviour of rigid plastics," ISO 6603-2:2000
33. Butt J, Bhaskar R, Mohaghegh V (2022) Analysing the effects of layer heights and line widths on fff-printed thermoplastics. The

International Journal of Advanced Manufacturing Technology 121(11–12):7383–7411

34. De Rosa S, Tammaro D, D'Avino G (2023) Experimental and numerical investigation of the die swell in 3d printing processes. Micromachines 14(2):329
35. Santhanakrishnan Balakrishnan V, Wartig K, Tsombanis N, Seidlitz H (2019)"Influence of processing parameters on the impact behaviour of glass/polyamide-6 composite," *Composites Part B: Engineering*, 159, 292–299
36. Crupi V, Epasto G, Guglielmino E (2016) Internal damage investigation of composites subjected to low-velocity impact. Experimental Techniques 40:555–568
37. Xie S, Wang C, Deng W (2020) Experimental study on collision acceleration and damage characteristics of potato. Journal of Food Process Engineering 43(9):e13457
38. Naik N, Ramasimha R, Arya H, Prabhu S, ShamaRao N (2001) Impact response and damage tolerance characteristics of glass-carbon/epoxy hybrid composite plates. Composites Part B: Engineering 32(7):565–574
39. Palomba G, Epasto G, Crupi V (2022) Lightweight sandwich structures for marine applications: a review. Mechanics of Advanced Materials and Structures 29(26):4839–4864
40. Detry ALHS, Landolfi L, Tammaro D, Lepore A, Villone MM, Maffettone PL, Squillace A (2024) Foam additive manufacturing of thermoplastic polymers: The influence of the process parameters. Journal of Manufacturing Processes 125:64–74
41. Bumbudsanpharoke N, Ko S (2015) Nano-food packaging: an overview of market, migration research, and safety regulations. Journal of food science 80(5):R910–R923
42. Youssef AM, El-Sayed SM (2018) Bionanocomposites materials for food packaging applications: Concepts and future outlook. Carbohydrate Polymers 193:19–27
43. Landolfi L, Detry ALHS, Cozzolino E, Tammaro D, Squillace A (2024) Energy-saving approach for mechanical properties enhancement of recycled pet additively manufactured by mex. Sustainable Materials and Technologies 41:e01038

Publisher's Note Springer Nature remains neutral with regard to jurisdictional claims in published maps and institutional affiliations.